# Y-faujasite encapsulated Co clusters: synthesis, characterization and theoretical model as probe of the methane homologation

James G.C. Shen*,** and Qisheng Ma

*Department of Chemistry, Zettlemoyer Center for Surface Studies, Lehigh University, Bethlehem, PA 18015, USA*

Received 2 July 2003; accepted 18 November 2003

The adsorption of $Co_2(CO)_8$ onto the dehydrated Y-faujasite powder under an $N_2$ atmosphere and onto the tetrahydrofuran slurry of Y-faujasite under a mixed CO and $H_2$ atmosphere predominately yielded supported $Co_4(CO)_{12}$ and supported $Co_6(CO)_{16}$, respectively. The molecular cobalt-carbonyl clusters and their decarbonylated products have been structurally characterized by extended X-ray absorption fine structure (EXAFS). The decarbonylated *sample a* possesses a cluster of two Co atoms and the decarbonylated *sample b* has a cluster phase of three Co atoms. The decarbonylated *sample a* exhibited higher $CH_4$ conversion and $C_{2+}$ selectivity ($C_{2+}$ selectivity $= \sum nC_n(n = 2\text{–}5)/\sum nC_n$ $(n = 1\text{–}5) * 100\%$) in comparison with the decarbonylated *sample b* in methane homologation. A density functional theory (DFT) model was employed to calculate Co clusters adsorbed on a silica substrate which simulates Y-faujasite encapsulated Co clusters. The structural geometries, net spin electronic charge densities, energies of the metal–silica and metal–metal interactions in stable geometries are discussed and used to interpret the cluster size dependence of the catalytic activity and selectivity to $C_{2+}$ hydrocarbons in the methane homologation.

**KEY WORDS:** Y-faujasite encapsulated Co clusters; decarbonylated Co clusters; EXAFS; methane homologation; $C_{2+}$ selectivity; density functional theory (DFT); net spin charge densities.

## 1. Introduction

Transition metal clusters supported on oxides have broad applications in heterogeneous catalysis, such as hydrogenation, dehydrogenation, hydrogenolysis, isomeration and amination [1–5]. In the past decade, properties of the aluminosilicate zeolites with well-defined channel, the pore nanostructure, large surface area and the high thermal stability, make them attractive supports for the preparation of the zeolite encapsulated metal clusters [6,7]. The synthesis routes to the encapsulated organometallic species inside the void spaces of zeolite involve chemical vapor deposition [8], metal ion exchange [7,9,10], vapor-phase impregnation [11], or carbonyl (photo)topotaxy [12] followed by reductive carbonylation under a mixed CO and $H_2$ atmosphere. Infrared spectroscopy and $^{23}Na$ NMR provided a direct picture of the interaction between metal carbonyl clusters and the site II $Na^+$ cations in supercages through involvement of the oxygen end of the carbonyl ligands [13]. The intrazeolite anchoring of metal carbonyl clusters as well as the interaction of metal clusters and the support medium, have been studied in detail and published [7–11,13]. In several successful cases, the decarbonylation of the intrazeolitic metal carbonyl clusters produced low loading of ''single-size'' quantized nano-clusters, such as $Ir_4$, $Rh_6$, $Ru_3$, $Ru_6$ locked within the void cavities of zeolite [7–11]. Such intrazeolitic bare metal clusters exhibited significant catalytic performances in CO hydrogenation, $CH_4$ homologation and aromatic hydrocracking reactions [3,14]. In these catalytic reactions, one realized that zeolite participated in the dispersion of metal clusters and zeolite structure contributed to product selectivities. None of the investigations hitherto available, however, has effectively addressed electron transfer or interactions in bare cluster atoms and the cluster-aluminosilicate, and a promotion pathway of zeolite in the catalysis. This is partly due to the complexity of the catalysis and the lack of characterization techniques. The enhancing catalytic effect of the cluster size and zeolite is often ignored.

In aluminosilicate zeolite supported transition metal catalysts, the cluster metal is superior to the bulk metal in catalytic activity and product selectivity which are sensitive to cluster sizes and interactions among cluster atoms [3a]. Experimental measurements by electron microscopies, such as XPS and STM, hardly provide insights into the relationship of the catalytic activity and cluster size/structure. On the other hand, quantum mechanical calculations, especially the density functional theory (DFT), have been widely applied to provide fundamental understanding in the experimental physicochemical properties of metal cluster catalysts, particularly in the metal-support interactions involving microelectronic phenomena. In this regard, we designed

*To whom correspondence should be addressed.
E-mail: jgcshen50@hotmail.com
**Present address: Specialty Minerals Inc. 9 Highland Avenue Bethlehem, PA 18017, USA.

1011-372X/04/0300–0019/0 

a theoretical model to simulate the interaction between Co clusters and the $SiO_2$ substrate based on the DFT calculations at the full-potential linearized augmented plane wave (FP-LAPW) level with the spin polarization taken into account.

Our research focuses on the synthesis of zeolite encapsulated nanoscopic metallic clusters through reductive carbonylation of vapor deposited organometallic species followed by decarbonylation. We aim at showing chemical properties of the aluminosilicate zeolite supported metal cluster catalysts through the example of the Y-faujasite supported Co clusters, and revealing geometrical and energetic properties as well as the interaction of cluster atoms and clusters-zeolite via the theoretical analysis of the density functional calculations.

In the second part of this study, the methane homologation over various size of Co clusters located within Y-faujasite pores is investigated to probe relevant details such as the Y-faujasite electron transition and clusters size effects in the catalysis.

## 2. Experimental section

### 2.1. Preparation of samples

#### 2.1.1. Sample a

The Y-faujasite powder (HSZ-320 NAA, Lot D1-9915, Si/Al = 3.1, surface area = 910 $m^2/g$) was dehydrated by evacuation at 623 K for 2 h, and was mixed mechanically with $Co_2(CO)_8$ (Stream Chemical, stabilized with 5–10% hexane) under an $N_2$ atmosphere at 300 K followed by aging for 1 h at 300 K to give the brown sample denoted as *sample a*.

#### 2.1.2. Sample b

The $Co_2(CO)_8$ was dissolved in dry deoxygenated tetrahydrofuran (THF), and then the dehydrated Y-faujasite pellet was immersed into the THF solution of $Co_2(CO)_8$ until the brown coloration of the THF/$Co_2(CO)_8$ solution disappeared. After removal of the solvent, the pellet was exposed to a $CO/H_2$ atmosphere ($CO/H_2$ = 300 Torr/100 Torr) in a U-type reactor at 298–313 K to give the black sample denoted as *sample b*.

The *samples a* and *b* were oxidized at 353 K followed reduced at 673 K, obtaining decarbonylated *samples a* and *b* as previously described [8b].

### 2.2. Characterization of samples

#### 2.2.1. EXAFS spectroscopy

EXAFS measurements were carried out at the Photon Factory in the Japan National Laboratory for High Energy Physics using synchrotron radiation with an electronic energy of 2.5 GeV at currents of 200–350 mA. The spectra at the Co k-edge (7.7 KeV) were measured at 296 K under vacuum using a Si(111) double-crystal monochromator. Analyses of EXAFS spectra were performed using the computer program EXAFS 2 [15]. The reference samples used were crystalline $Co_4(CO)_{12}$, $Co_6(CO)_{16}$, $Co_3O_4$ and Co foil.

#### 2.2.2. EXAFS data analysis

The EXAFS data was extracted from the measured absorption spectra by standard methods [15,16]. The normalization was done by dividing the absorption intensities by the height of the absorption edge and subtracting the background using cubic spline routines. The final EXAFS function was obtained by averaging the individual background-subtracted and normalized EXAFS data (two scans for each sample). The main contributions to the spectra were isolated by inverse Fourier transformation of the final EXAFS function over a selected range in the *R*-space (*R* is the distance from the absorption atom). The analysis was performed on these Fourier-filtered data using empirical parameters (the phase shift and backscattering amplitude functions) obtained from reference samples. The parameters characterizing high-*Z* (Co) and low-*Z* (C, O) contributions were reliably determined by multiple-shell fitting in the *k* space (*k* is wave vector) and the *R* space with an application of $K^3$ weighting of the Fourier transform. The accuracy of the parameters was estimated as $0.02 < \sigma < 0.08$ and $-10 < \Delta E^o < 10$. The residual factor $\int|k^3\chi^{obs}(k) - k^3\chi^{calc}(k)|^2 dk / \int|k^3\chi^{obs}(k)|^2 dk$ was less than 15% for optimized coordination numbers and bond lengths [15].

### 2.3. Methane homologation

The decarbonylated *samples a* and *b* were placed into the reactor, respectively, and flushed adsorbed $H_2$ with He at 300 K for 30 min. The temperature of the reactor was raised under flowing He, and then switch to a pulsed gas containing dilute $CH_4$ by He. After methane dissociation, the decarbonylated sample was quickly cooled to room temperature under He flowing to avoid aging of the surface carbonaceous deposits. The surface carbonaceous deposits were subsequently hydrogenated in a $H_2$ flow of 20 $cm^3$ (STP)/min from 298 to 673 K. Before entering the catalyst bed, the gases (He, $CH_4$ and $H_2$) were purified through manganese oxide and molecular sieve. The effluent gases from the reactor were stored in loops and were determined afterward by Shimadzu GC-8A gas chromatography with a flame ionization detector.

### 2.4. Theoretical computations for the decarbonalated samples of Co atoms adsorbed on the $SiO_2$ substrate

The DFT calculations were performed at the FP-LAPW level as implemented in the WIEN 97.9 program [17]. A four-layers slab with a stacking-order of O—Si—O—H was created to model the silica surface with a stoichiometry $O_{3(top)}Si_2(OH)_2$ in the hexagonal

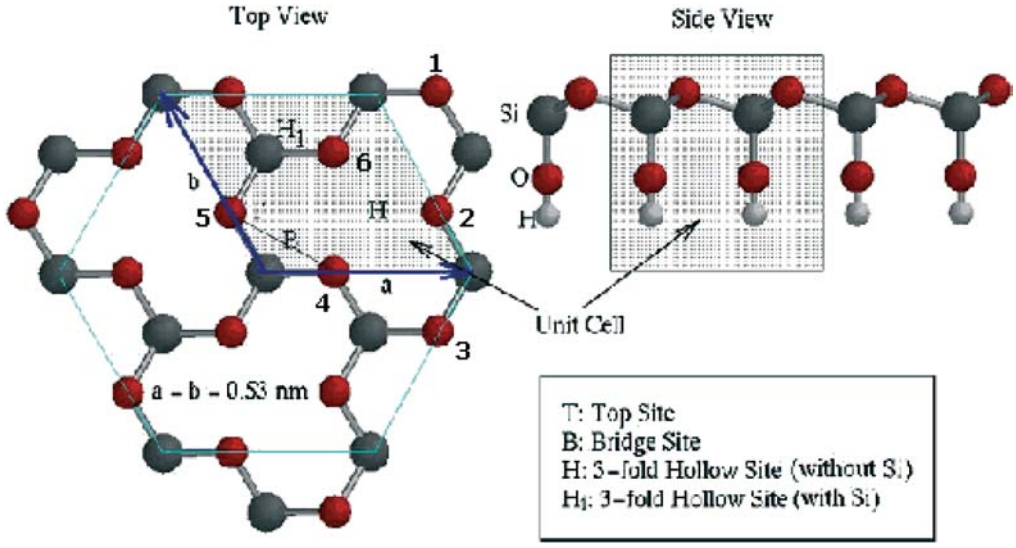


Figure 1. Silica surface structure. Shaded area represents a unit cell. The different adsorption sites are labeled as T (top), B (bridge), H (3-fold hollow O site), and $H_1$ (3-fold O above Si).

unit cell [18]. Such structural model contains three oxygen atoms to form a three-fold $C_{3v}$ axis in the top-layer. The second-layer Si maintains a six-ring framework window with each silicon atom forming nearly tetrahedral bonds to four nearest oxygen neighbors. The additional hydrogen layer is added to maintain a charge-neutral cell as a termination of the slab [18]. The internal coordinates of the slab were fully optimized to obtain minimum energy (1.36 eV) structure than that of the hexagonal structure. This structure exhibits considerable lattice relaxation, and both top view and side view were illustrated in figure 1. From top view, three (labeled 2, 4 and 6 in figure 1) of six O atoms closely move to the center of the six-Si member ring to form a perfect 3-fold triangle, while the other three O atoms (labeled 1, 3 and 5 in figure 1) pushed away from the center. Such structure is similar with —Si(Al)O-member ring of $\beta$-cage window in Y-faujasite subject to a substantial structural relaxation. The effect of the H of slab to the adsorbed metal is expected to be negligible because the H atoms are far away from the adsorption regions (7–8 Å). The geometry of adsorbed Co cluster is expressed by distances of the Co atoms to the nearest three oxygen atoms denoted as Co—$O_1$, Co—$O_2$ and Co—$O_3$, and their average distance was calculated. The energetic properties of the Co adsorption are described by the Co adsorption energy $E_{\mathrm{Co}}^{\mathrm{ads}}[n]$ as

$$E_{\mathrm{Co}}^{\mathrm{ads}}[n] = (1/n)(E_{\mathrm{Co}n}^{\mathrm{ads}} - E_{\mathrm{sub}} - E_{\mathrm{Co1}}) \qquad (1)$$

where $E_{\mathrm{Co}n}^{\mathrm{ads}}$ is total energy of $n$ Co atoms in the unit cell of the adsorbate-substrate system, $E_{\mathrm{sub}}$ is energy of the $SiO_2$ substrate alone, and $E_{\mathrm{Co1}}$ is the single atom energy calculated with one Co atom in a $1 \times 1 \times 1$ nm$^3$ unit cell. Here the $E_{\mathrm{Co}}^{\mathrm{ads}}[n]$ measures the adsorption strength, which includes the cobalt-substrate as well as Co—Co interaction.

The Co cluster adsorption energy $E_{\mathrm{Cluster}}^{\mathrm{ads}}[n]$ is defined as

$$E_{\mathrm{Cluster}}^{\mathrm{ads}}[n] = E_{\mathrm{Co}n}^{\mathrm{ads}} - E_{\mathrm{sub}} - E_{\mathrm{Co}n}^{\mathrm{free}} \qquad (2)$$

where $E_{\mathrm{Co}n}^{\mathrm{free}}$ is the total energy of the "free" Co cluster, and obtained by optimizing structure of the Co cluster [19]. Therefore the Co cluster adsorption energy $E_{\mathrm{Cluster}}^{\mathrm{ads}}[n]$ measures the ability of adsorption of a preformed Co cluster on the substrate, which reflects the cobalt-substrate interaction alone.

In addition, the one Co adsorption energy,

$$E_{\mathrm{Atom}}^{\mathrm{ads}}[n] = E_{\mathrm{Co}n}^{\mathrm{ads}} - E_{\mathrm{Co}n-1}^{\mathrm{ads}} - E_{\mathrm{Co1}} \qquad (3)$$

is defined to measure the energy associated with the addition of one atom to the adsorbed Co cluster.

## 3. Results and discussion

### 3.1. The characterization of the cobalt-carbonyl clusters by EXAFS spectroscopy

Infrared and diffuse reflectance spectroscopies show that the *sample a* is predominately $Co_4(CO)_{12}$/Y-faujasite, and the *sample b* is mainly $Co_6(CO)_{16}$/Y-faujasite [8b]. To obtain more insights into the structure of the Co carbonyl cluster in the samples, especially into the metal framework, the EXAFS spectra of the Co *k*-edge were analyzed. The EXAFS function was normalized by division by the height of the absorption edge. The raw EXAFS data characterizing *sample a* (figure 2, part Aa) and *sample b* (figure 2, part Ba), respectively, show oscillations up to the value of $k$, the wave vector, of about 12.5 and 13 Å$^{-1}$. This indicates the presence of near-neighbor high-atomic-weight backscatterers, which are inferred to be Co. Since the infrared spectra indicate that the carbonyl ligands were also present in the *samples a* and *b* [8b], the data were analyzed for Co—Co

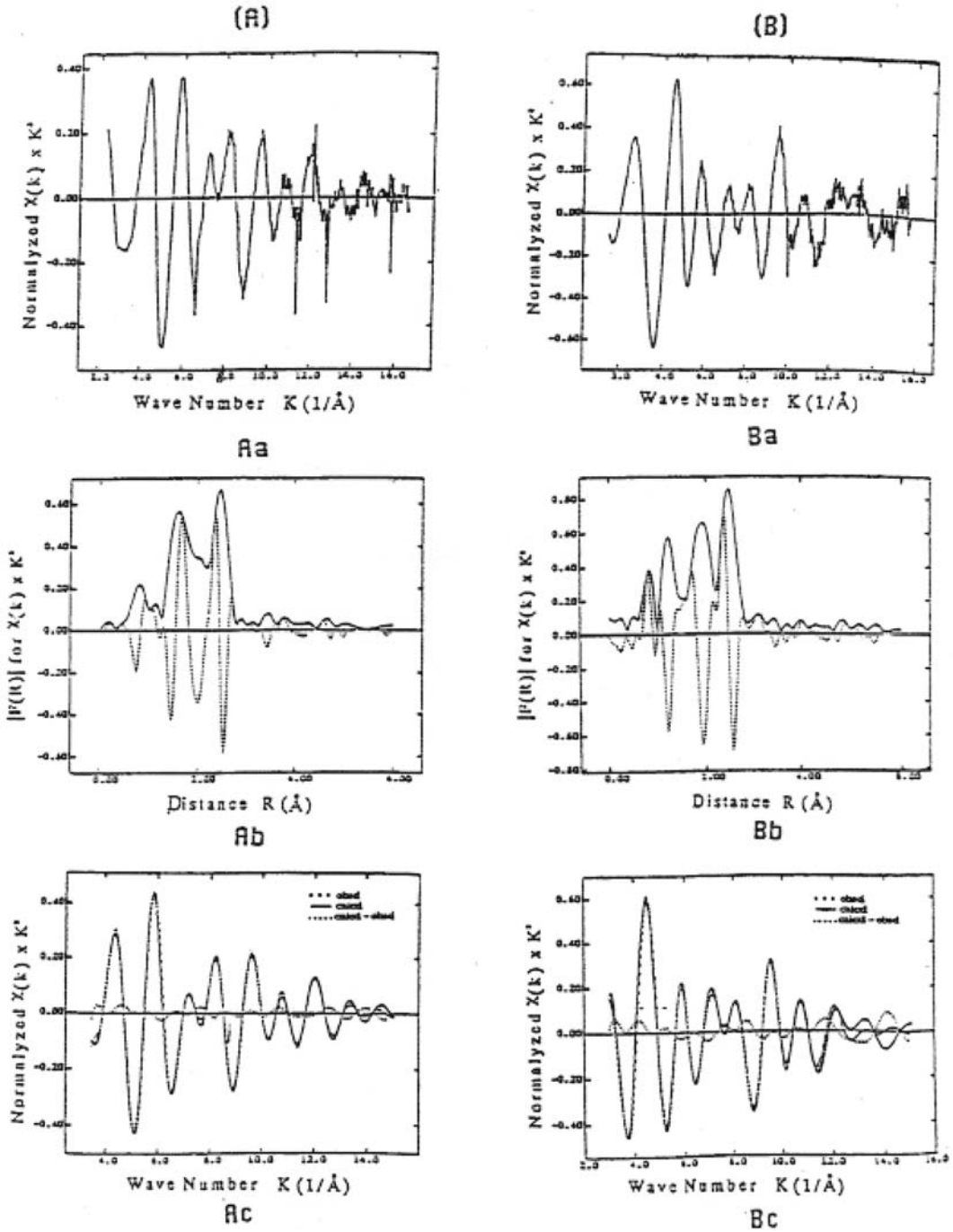


Figure 2. Results of EXAFS with best calculated coordination parameters characterizing *samples a* and *b*. (parts Aa-Ba) $K^2$-weighted EXAFS spectrum $K^2\chi(k)$ versus κ; (parts Ab-Bb) Fourier transform |FT| of $k^2$-weighted EXAFS spectrum $K^2\chi(k)$ versus $R$; (part Ac-Bc) inverse Fourier transform of experimental EXAFS in range $1.3 < R < 2.8$ Å and $1.2 < R < 3.0$ Å (dashed curve) and sum of the calculated Co—Co + Co—C + Co(—C—)O contributions (solid curve).

and Co—CO interactions. The raw EXAFS data characterizing *samples a* and *b* were Fourier transformed with a $K^2$-weighting over the range $2.0 < K < 16.0$ $Å^{-1}$ and in the range $5.0 < K < 16.0$ $Å^{-1}$, respectively. Figure 2, parts Ab and Bb exhibits peaks in the range of $1.3 < R < 2.8$ Å and in the range of $1.2 < R < 3.0$ Å (where $R$ is the distance from the adsorbed Co atom) attributable to Co—Co, Co—C and Co(—C—)O contributions. The Fourier-transformed data were then inverse Fourier-transformed in the range of $1.3 < R < 2.8$ Å (*sample a*) and in the range of $1.2 < R < 3.0$ Å (*sample b*) to isolate the major contribution from low-frequency and higher-shell contributions. The results of the curve-fitting analyses are

Table 1
Results of the curve-fitting analysis of Co-edge EXAFS data obtained at 296 K for samples[a]

| Samples | Co—Co | | | | Co—C | | | | Co(—C—)O | | | |
|---|---|---|---|---|---|---|---|---|---|---|---|---|
| | CN | $R$(Å) | $\Delta E_0$(eV) | $\sigma$(eV) | CN | $R$(Å) | $\Delta E_0$(eV) | $\sigma$(eV) | CN | R(Å) | $\Delta E_0$(eV) | $\sigma$(eV) |
| *Sample a* | 2.6 | 2.52 | −10.87 | 0.027 | 2.62 | 1.80 | 11.79 | 0.085 | 2.54 | 2.92 | −6.93 | 0.064 |
| *Sample b* | 3.0 | 2.51 | −11.88 | 0.051 | 2.90 | 1.81 | −7.06 | 0.081 | 2.60 | 2.94 | −4.11 | 0.060 |
| Decarbonylated *sample a* | 1.1 | 2.56 | 11.60 | 0.037 | | | | | 3.50 | 2.01 | 3.08 | 0.026 |
| Decarbonylated *sample b* | 2.0 | 2.50 | 7.53 | 0.046 | | | | | | | | |
| | 2.6 | 2.86 | −9.74 | 0.023 | | | | | 3.70 | 1.90 | 2.13 | 0.049 |
| | 3.9 | 3.36 | 13.23 | 0.034 | | | | | | | | |
| Ref samples | | | | | | | | | | | | |
| Co foil | 12.0 | 2.50 | 0.29 | 0.020 | | | | | | | | |
| $Co_4(CO)_{12}$ | 3.0 | 2.50 | −10.09 | 0.038 | 2.63 | 1.84 | 12.14 | 0.075 | 2.50 | 2.90 | −8.32 | 0.061 |
| $Co_6(CO)_{16}$ | 3.8 | 2.50 | −2.34 | 0.079 | 2.80 | 1.82 | 8.98 | 0.067 | 2.63 | 2.92 | −2.15 | 0.067 |
| $Co_3O_4$ | 4.0 | 2.85 | −11.67 | 0.047 | | | | | 5.40 | 1.90 | 11.19 | 0.051 |
| | 9.3 | 3.40 | −10.89 | 0.050 | | | | | | | | |
| CoO[b] | | | | | | | | | 8.0 | 2.13 | | |

[a] Notation: CN, coordination number for adsorber-backscatterer pair; $R$, radial adsorber-backscatterer distance; $\sigma$, Debye–Waller factor; $\Delta E_0$, inner potential correction (correction of the edge position).
[b] Reference [20].

shown in figure 2, part Ac and Bc, and table 1. The EXAFS results provide the strongest evidence that the backscatterers in the immediate vicinity of the Co absorber atoms include Co, and low-atomic-weight backscatters identified as C and O. The relative contributions of these backscattering atoms support the identification of the Y-faujasite-entrapped species as $Co_4(CO)_{12}$ for the *sample a* and $Co_6(CO)_{16}$ for the *sample b*.

The EXAFS results characterizing the *samples a* and *b* were in fair agreement with the crystallographic data for $Co_4(CO)_{12}$ and $Co_6(CO)_{16}$, respectively (table 1). The data indicate Co—Co coordination numbers of 2.6 with an average Co—Co distance of 2.52 Å, Co—C coordination of 2.62 with an average Co—C distance of 1.80 Å, and Co(—C—)O coordination numbers of 2.54 with an average Co(—C—)O distance of 2.92 Å for the *sample a*; the results also show Co—Co coordination numbers of 3.0 with an average Co—Co distance of 2.51 Å, Co—C coordination numbers of 2.90 with an average Co—C distance of 1.81 Å, and Co(—C—)O coordination numbers of 2.60 with an average Co(— C—)O distance of 2.94 Å for the *sample b*. On the other hand, the discrepancy between the Co—Co coordination numbers of the samples and crystalline cobalt-carbonyl clusters with a $N$(Co—Co) ratio of 2.6:3.0 for *sample a*/$Co_4(CO)_{12}$, and a $N$(Co— Co) ratio of 3.0:3.8 for *sample b*/$Co_6(CO)_{16}$ implies that about 90% of the Co atoms are present as $Co_4(CO)_{12}$ clusters for the *sample a* and about 80% of Co atoms are present as $Co_6(CO)_{16}$ clusters for the *sample b*. The calculation of the coordination number for the samples was in agreement with the abundance of $Co_6(CO)_{16}$ and $Co_4(CO)_{12}$ species in the samples calculated from the area of the respective peaks in the infrared spectra [8b].

### 3.2. The characterization of the decarbonylated cobalt clusters by EXAFS spectroscopy

The *samples a* and *b*, were oxidized and followed reduced by $H_2$ at 673 K for 6 h, obtaining the decarbonylated *samples a* and *b*. EXAFS data indicated that the decarbonylated *sample a* possesses a Co—Co bond at an average distance of 2.56 Å (coordination numbers of 1.1), loss of CO ligands, and a new species with a Co—O bond at an average distance of 2.01 Å, with coordination numbers $N$(Co—O) of 3.50. This Co—O distance is shorter than the 2.13 Å distance of the CoO crystal and longer than the 1.90 Å distance of the $Co_3O_4$ crystal as shown in table 1 [20]. A plausible structure for the decarbonylated *sample a* is a two Co atoms phase and a $[CoO]_n$ saltlike phase in Y-faujasite cages [8b,20].

Table 1 presents EXAFS parameters of the decarbonylated *sample b*. The metal species with the Co—Co coordination number $N = 2.03$ at an average distance of 2.50 Å, and an oxide phase with a Co—O bond at an average distance of 1.90 Å (coordination numbers of 3.70) and with Co—Co bond at an average distance of 2.86 Å ($N = 2.60$) and 3.36 Å ($N = 3.90$), have been identified. The average Co—O and Co—Co distances are similar with that in the bulk spinal $C_3O_4$, but the smaller coordination numbers for Co—Co bonds of the oxide phase are in contrast with those of bulk spinal $Co_3O_4$ (table 1). This suggests a raftlike structure for $[Co_3O_4]_n$ on Y-faujasite [20]. Thus, the decarbonylated *sample b* consists a three Co atom

Table 2
Kinetic parameters of methane homologation on the Y-faujasite encapsulated Co cluster catalysts[a]

| Samples | $CH_4$ dissociation temp. (K) | $C_1$(%) | $\theta$ [$CH_x$/Co] | $C_2$ (%) | $C_{2+}$ (%)[b] | $C_1xC_2$(%) | $C_1x(1\text{-}C_2)$ (%) |
|---|---|---|---|---|---|---|---|
| Decarbonylated sample a | 623 | 18.7 | 0.13 | 74.4 | 20.6 | 13.8 | 4.80 |
| | 723 | 30.7 | 0.22 | 39.6 | 16.7 | 12.2 | 18.5 |
| Decarbonylated sample b | 623 | 11.2 | 0.08 | 56.4 | 8.8 | 7.3 | 4.90 |
| | 723 | 23.0 | 0.17 | 28.5 | 6.4 | 6.6 | 16.4 |

[a] 100 mg decarbonylated *sample a* or decarbonylated *sample b*; step1: exposure of the catalyst to 0.02 mmol $CH_4$ at 623 or 723 K; step 2: hydrogenation of adspecies by a $H_2$ flow of 20 $cm^{-3}$ STP $min^{-1}$ from 300 to 673 K.
[b] $C_{2+}$ selectivity = $\sum nCn(n = 2\text{–}5)/\sum nCn$ ($n$ = 1–5).

cluster phase and a raftlike $[Co_3O_4]_n$ phase in Y-faujasite cages.

### 3.3. Methane homologation depending on the Co cluster size

The methane homologation was carried out in a two-step procedure by the thermal dissociation of methane on the decarbonylated *samples a* and *b*, followed by the hydrogenation of the surface species deposited on the cluster surface [3a,8a]. Methane and all hydrocarbon products were determined by GC with a flame ionization detector. Table 2 lists the kinetic parameters of the methane homologation on the decarbonylated *samples a* and *b*. These include methane converted to carbonaceous deposits ($C_1$) and the carbonaceous surface coverage ($\theta$) in the methane dissociation as well as the carbonaceous deposits converted to hydrocarbons ($C_2$) and $C_{2+}$ selectivity ($C_{2+}$ selectivity = $\sum nC_n(n = 2\text{–}5)/\sum nC_n$ ($n$ = 1–5) * 100%) in the hydrogenation of the carbonaceous deposits. To balance the carbons in the reactions, we estimated the methane conversion to the hydrocarbons by multiplying $C_1$ and $C_2$ and residual carbonaceous deposits by multiplying $C_1$ and (1-$C_2$). For the decarbonylated *samples a* and *b* at the $CH_4$ dissociation temperature of 723 K, $C_1$ is 30.7% and 23.0%, respectively; the carbonaceous surface coverage ($\theta$) is 0.22 on the decarbonylated *sample a* and 0.17 on the decarbonylated *sample b*; $C_2$ reaches 39.6% for the decarbonylated *sample a* and 28.5% for the decarbonylated *sample b*; the $C_{2+}$ selectivity is 16.7% for the decarbonylated *sample a* and 6.4% for the decarbonylated *sample b*; The $C_1 \times C_2$ is 12.2% on the decarbonylated *sample a* and 6.6% on the decarbonylated *sample b*.

It is not known whether the catalytic properties of metallic particles are size-dependent as the particles are too small (diameter <10 Å). Here, we investigated the catalytic behavior of precisely defined clusters of just 2 and 3 Co atoms in Y-faujasite cages, and determined their catalytic activity. The cobalt oxide phase in either the decarbonylate *sample a* or the decarbonylated *sample b* is not active species for the methane homologation [3a,8a]. The decarbonylated *sample b* with three Co atom cluster was 1.8 times less active ($C_1 \times C_2$) and had 2.6 times lower $C_{2+}$ selectivity than the decarbonylated *sample a* with two Co atom cluster phase.

### 3.4. Theoretical model of Co atoms adsorbed on $SiO_2$ substrate simulated the decarbonylated samples as a probe of the activity and selectivity in the methane homologation

#### 3.4.1. Cobalt adsorption geometry

The methane homologation data suggests that the catalytic properties of the Y-faujasite supported Co clusters are metal-size-dependent. Due to the lack of experimental characterization technique in exploring the role of cluster size in the catalysis and promotion pathway of Y-faujasite support, we established a theoretical model of Co clusters adsorbed on the $SiO_2$ slab. Y-faujasite possesses a 6-member ring of the Si(Al)—O alternate as window of the $\beta$-cage and a 12-member ring of the Si(Al)—O alternate as window of the $\alpha$-cage as well as a Si/Al = 3.1 molar ratio [7]. The metal Co cluster is close to the six-membered ring of the $\beta$-cage aperture in the decarbonylated samples [7,8b]. We simulated the $\beta$-cage window of the six-membered ring of —Si(Al)—O— alternate by the minimum energy structure of stoichiometry $O_{3(top)}Si_2(OH)_2$ (figure 1) (where Al atoms in Y-faujasite were replaced by Si atoms).

The decarbonylated *sample a* contains two Co atoms in each cluster phase, which was simulated by a side-on configuration and calculated by starting with two Co atoms near the silica surface. The geometry optimization for two Co on the $SiO_2$ substrate yielded a minimum energy structure as illustrated in figure 3a. Two Co atoms lie nearly parallel to the top layer of the $SiO_2$ substrate and the Co atoms located closer to two on-top (T) sites (figure 3a). The Co adsorption energy $E_{Co}^{ads}[2] = -3.98$ eV, resulted from the Co—Co interaction (Co—Co distance of 2.19 Å) and cobalt-substrate interactions (table 3). The distances of the Co atom A (labeled A in figure 3a) to the nearest three oxygen atoms are 2.09, 2.96 and 3.43 Å at an average 2.83 Å, and the distances of the Co atom B (labeled B in figure 3a) to the nearest three oxygen atoms are 2.10, 3.19 and 3.23 Å at an average 2.84 Å, as listed in table 3.

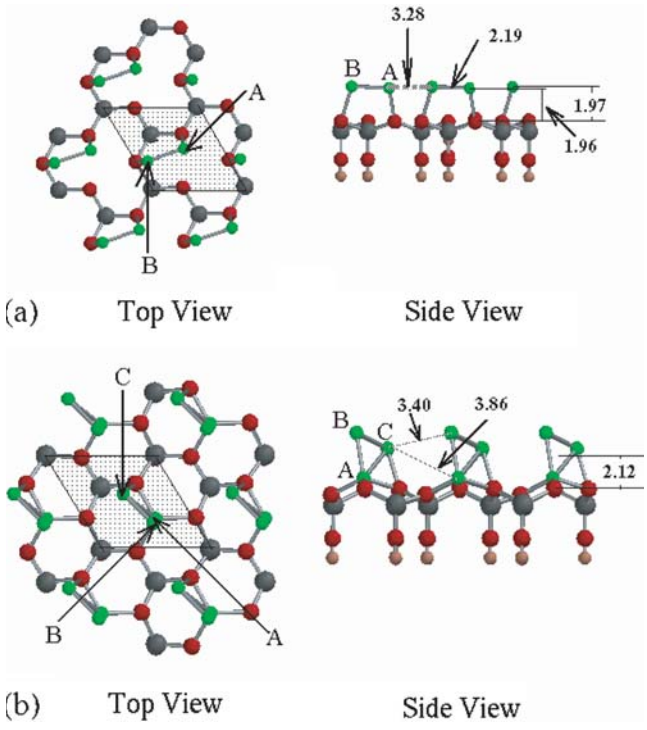


Figure 3. (a) Surface configuration of $Co_2$ clusters adsorbed on the silica substrate with Co:O = 2/3 ratio, shows both the top view and the side view. (b) Geometry of $Co_3$ clusters adsorbed on the silica substrate with Co:O = 3/3 ratio. Atom color code as follows: Co, green; O, red; Si, black; and H, red–yellow.

Table 3
Geometry of Co clusters on the silica substrate

| Co: O ratio | Geometry (Å) | | | |
|---|---|---|---|---|
| | Average $Co_A$—O | Average $Co_B$—O | Average $Co_C$—O | Average Co—Co |
| 2:3 | 2.83 | 2.84 | | 2.19 |
| 3:3 | 2.01 | 3.43 | 2.84 | 2.29 |

The decarbonylated *sample b* involves three Co atoms in each metal cluster phase. A stable configuration with the optimized geometry was simulated when 3 Co atoms were adsorbed per unit cell, where the Co atoms with top oxygen and second layer silicon atoms were relaxed. The first two Co atoms remained nearly in their stand-up configuration (labeled A, B in figure 3b), while the third Co atom adsorbed near the on top T site (labeled C in figure 3b). Three Co atoms formed a triangular cluster with Co—Co distances of 2.14, 2.20 and 2.82 Å with an average $d$(Co—Co) = 2.29 Å, as presented in table 3. The average distance of the Co atom A, B and C to the nearest three oxygen atoms is 2.01, 3.43 and 2.84 Å, respectively (table 3).

### 3.4.2. Cobalt adsorption energies and spin states

The cluster properties are determined by the interplay between adsorption energies and metal–metal interactions. As the cluster size increases, the nearest distance of Co to the top oxygen-plane dramatically increases from ~0.8 Å for a single adsorbed Co atom to >4.0 Å for a supra-monolayer. The Co—Co distance is ~2.2 Å in the stable adsorbed dimers, but ~2.3 Å when cluster growth to stable trimers and tetramers (Table 3). These Co—Co distances are close but smaller than 2.5 Å of the decarbonylated samples *a* and *b* by EXAFS measurement (table 1) and the bulk hcp Co metals [8b,20,21].

The total clusters, the structural patterns and adsorption energies exhibit a trend, as shown in figure 4. The adsorption energy per Co atoms defined by equation 1, $E^{ads}_{Co}[n]$, increases with the cluster size, primarily due to the Co—Co bond formation (table 3). Simultaneously, the adhesion energy of the Co clusters to the $SiO_2$ substrate defined by equation 2, $E^{ads}_{Cluster}[n]$, decrease with the cluster size. The adsorption energy of a single Co atom onto a precursor cluster defined by equation 3, $E^{ads}_{Atom}[n]$, slightly decreases with cluster growth from two Co atoms to three.

The electronic charge density of the clusters in the DFT calculation was decomposed into the spin-up ($\rho_\alpha$) and spin-down ($\rho_\beta$) components through spin-polarization calculations [18]. The total charge density $\rho$ is equal to $\rho_\alpha + \rho_\beta$, and the net spin density is defined as $\rho_{spin} = \rho_\alpha - \rho_\beta$. The silica substrate without the presence of Co metal is spin-free ($\rho_{spin} = 0$), while the Co atom has $\rho_{spin} = 3$ with 5 spin-up d electrons and 2 spin-down d electrons in its atomic state, and a doubly occupied, spin-paired 4s shell. figure 5 represents graphically the calculated total charge densities $\rho$ and the net spin densities $\rho_{spin}$ of selected Co atoms adsorbed on the silica substrate. Overall, the net spin densities are distributed among the Co atoms, with a relatively small portion density extended into the top-layer oxygen atoms of the silica substrate. This suggests that the presence of the Co clusters polarize the silica surface. The extending of net spin density decreases with increasing cluster size (figure 5). This is corresponding to increase of the net spin density among the cluster with the cluster size growth on the silica substrate. The Co—Co interactions are much more dependent on the distribution of net spin densities. As seen from net spin density in figure 5a, an antibonding $\sigma$*-like bond was formed with a node between the two Co atoms.

The theoretical calculation using a two-dimensional periodic slab model, $Co_nO_{3(top)}Si_2(OH)_2$ composition, demonstrated several parameters involving the structural geometries, net spin densities, energies of the cobalt-silica and Co—Co interaction in stable geometries. These parameters could respond to the catalytic activity and the product selectivities in the methane homologation. The net spin charge densities and the adsorption energy of each Co atom, $E^{ads}_{Co}[n]$ are elevated with increasing cluster size, which corresponded to decrease of the methane conversion and $C_{2+}$

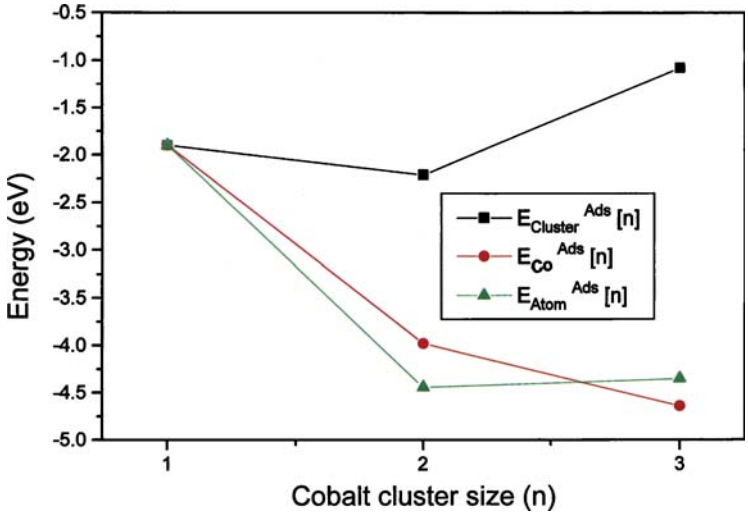


Figure 4. Energy relations versus the clusters size. The adsorption energies $E^{ads}_{Co}[n]$, $E^{ads}_{Cluster}[n]$ and $E^{ads}_{Atom}[n]$ were defined in equations (1)–(3).

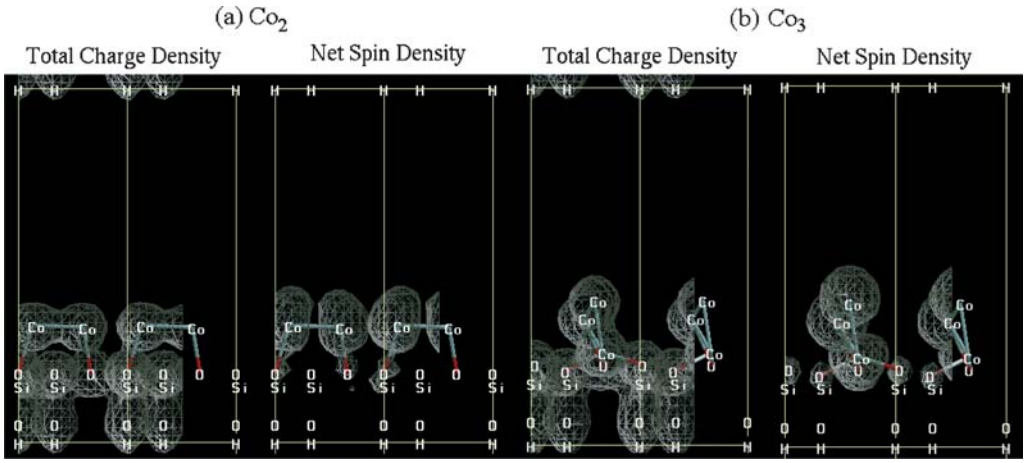


Figure 5. Total charge densities and net spin densities of selected Co atoms adsorbed on the silica substrate. (a) Two Co atoms adsorbed in the side-on configuration and (b) three Co atoms adsorbed with substrate relaxed. The projected side view renditions with 2-times of the unit cell are presented. The electric densities cover 11/2 unit cell from the left with a bare 1/2 unit cell from the right in each figure.

hydrocarbon selectivities in the methane homologation (figure 4 and table 2).

In the methane homologation reaction, the surface carbonaceous fragments are the intermediate species for the hydrocarbon formation, which are identified to be $CH_x$ ($x = 0, 1, 2$) based on the analyses of temperature-programmed hydrogenation (TPH), and FT-IR and mass spectroscopies of carbonaceous deuteration [3a,8a]. The chain-growth probability of the hydrocarbon depend on the $CH_x$ mobility on the metal cluster surface [22]. The increase of net spin charge densities resulted in the enhancement of Co—$CH_x$ interaction and reduce of mobility of $CH_x$ species on the Co clusters surface with increasing cluster size. Therefore, high $CH_4$ conversion and selectivity to $C_{2+}$ hydrocarbons were efficiently produced on the decarbonylated *sample a* which possesses smaller Co cluster size, lower Co—$CH_x$ reactivity, higher mobility of $CH_x$ intermediate species, and higher chain-growth probability in comparison with the decarbonylated *sample b*.

## 4. Conclusions

The research encompassed several key points as follows.

(i) Molecular cobalt-carbonyl clusters and their decarbonylated samples have been structurally characterized by EXAFS spectroscopy. The results indicate that $Co_4(CO)_{12}$ and $Co_6(CO)_{16}$ were synthesized in Y-faujasite cages, and their decarbonylated species maintain small Co cluster size. (ii) Methane homologation was carried out on Y-faujasite supported Co clusters using a two-step process. The catalytic activity and selectivity to $C_{2+}$ hydrocarbons exhibited the dependence of cluster size. (iii) The simulated model of Co

clusters adsorbed on silica substrate with minimum energy structure of stoichiometry $O_{3(top)}Si_2(OH)_2$, replicated the structure of Co cluster located in Y-faujasite $\beta$-cage in the synthesized *samples a and b*. (iv) The net spin charge density of the simulated Co atoms adsorbed on silica substrate exhibited enhancement with increasing cluster size, which respond to the Co cluster size dependence of $CH_4$ conversion and $C_{2+}$ selectivity in the methane homologation.

## References


[1] J.H. Sinfelt, Bimetallic Catalysts, Discoveries, Concepts, and Application; Exxon Monograph; (Wiley, New York, 1983).
[2] B.C. Gates, L. Guczi, and H. KnÖzinger, (eds.) Metal Clusters in Catalysis (Elsevier, Amsterdam, 1986).
[3] (a) J.G.C. Shen, A.M. Liu, T. Tanaka and M. Ichikawa, J. Phys. Chem. B 102 (1998) 7782. (b) G.C. Shen, A.M. Liu, T. Shido and M. Ichikawa, Top. Catal. 2 (1995) 141.
[4] M. Ichikawa, Adv. Catal. 38 (1992) 283.
[5] G.S. Swell, C.T. O'Connor and E. van Stern, Appl. Catal. A 125 (1995) 99.
[6] G.A. Ozin and C. Gil, Chem. Rev. 89 (1989) 1749.
[7] J.G.C. Shen, A.M. Liu, M. Ichikawa, Inorg. Chem. 37 (1998) 5497.
[8] (a) J.G.C. Shen, J. Phys. Chem. B 104 (2000) 423. (b) G.C. Shen, T. Shido and M. Ichikawa, J. Phys. Chem. 100 (1996) 14265.
[9] J.G.C. Shen, A.M. Liu and M. Ichikawa, J. Chem. Soc., Faraday Trans. 94 (1998) 1353.
[10] L.L. Sheu, H.K. Knözinger and W.M.H. Sachtler, J. Am. Chem. Soc. 111 (1989) 8125.
[11] (a) S. Kawi, J.R. Chang and B.C. Gates, J. Am. Chem. Soc.115 (1993) 4830. (b) S. Kawi, J.R. Chang and B.C. Gates, J. Phys. Chem. 97 (1993) 5375. (c) T. Beutel, S. Kawi, S.K. Purnell, H.K. Knözinger and B.C. Gates, J. Phys. Chem. 97 (1993) 7284.
[12] G.A. Ozin and S. Özkar, J. Phys. Chem. 94 (1990) 7556.
[13] J.G.C. Shen, J. Phys. Chem. B. 105 (2001) 2336.
[14] (a) T.F. Degnan, Jr, K.M. Keville, M.E. Landis, D.O. Marler and D.N. Mazzone, US Patent 5, 183 (1994) 557, assigned to Mobil Corp. (b) C.D. Chang, S. Han, D.J. Martenak, J.G. Santiesteban and D.E. Walsh, US Patent 6, 217 (2001) 747, assigned to Mobil Corp.
[15] N. Kosugi and H. Kuroda, Program EXAFS 2; Research Center for Spectrochemistry, University of Tokyo, 1988.
[16] J.B.A.D. van Zon, D.C. Koningsberger, H.F.J. van't Blik and D.E. Sayers, J. Chem. Phys. 12 (1995) 5742.
[17] P. Blaha, K. Schwarz and J. Luitz, WIEN 97, A Full Potential Linearized Augmented Plane Wave Package for Calculating Crystal Properties; Technische Universität: Wien, Austria, 1999.
[18] Q. Ma, K. Klier, H. Cheng, J. Mitchell and K. Hayes J. Phys. Chem. B, 104 (2000) 10618.
[19] V. Musolino, A. Selloni and R. Car, Surf. Sci. 413 (1998) 402.
[20] Y. Iwasawa, M. Yamada; Y. Sato and H. Kuroda, J. Mol. Catal. 23 (1984) 95.
[21] P. Chini, J. Chem. Soc., Chem. Commun. (1967) 440.
[22] H. Yang and J.L. Whitten, Surf. Sci. 255 (1991) 193.